Int. J. Electrochem. Sci., 17 **(2022)** Article Number: 220936, doi: 10.20964/2022.09.31

International Journal of
ELECTROCHEMICAL
SCIENCE
www.electrochemsci.org

Experimental Investigation of Proton Exchange Membrane Fuel Cell with Commercial Stainless Steel Fiber Felt as Flow Field

Guangxuan Lu[*], *Peng Ge, Qinlong Hou, Biying Ren, Xiangkun Jia, Qiang Liao*

Western Metal Materials Co., Ltd., Xi'an 710201, China
[*]E-mail: luguangxuan2019@outlook.com

Received: 24 May 2022 / *Accepted:* 29 June 2022 / *Published:* 7 August 2022

Porous metal materials have been recognized as a promising substitute for the conventional ribchannel flow field of proton exchange membrane fuel cell (PEMFC). Few studies have been reported on metal fiber felts as PEMFC flow fields, although they have many favorable properties. In this work, the structure feasibility of metal fiber felts as flow fields of PEMFC is explored experimentally. Five types of gold-plated commercial stainless steel fiber felts (CSSFFs) are investigated and compared with conventional serpentine flow field. The results indicate that the performances of fuel cells with CSSFF flow fields are improved significantly. In particular, fuel cell with BZ100D flow field performs the best among all CSSFFs, generating about 2.0 $A \cdot cm^{-2}$ at 0.6 V, and the maximum power density is approximately 1.25 $W \cdot cm^{-2}$ at 2.5 $A \cdot cm^{-2}$. This work verifies that CSSFFs with conductive and corrosion resistant coating can be viable alternatives to conventional rib-channel flow field.

Keywords: Proton exchange membrane fuel cell; Flow field; Metal fiber felt; Stainless steel fiber felt

1. INTRODUCTION

Proton exchange membrane fuel cell (PEMFC) is a device that can directly transform the chemical energy of fuel and oxidant to electrical energy through electrochemical reactions. PEMFC is considered as one of the most promising power sources for transportation applications such as automobiles, buses, ships and air vehicles because of its advantages including high efficiency, environmental friendliness, relatively low operating temperature, etc. [1-3] The main components of a typical PEMFC stack include membrane electrode assembly (MEA), bipolar plates, gaskets and end plates, among which a 7-layer MEA is consisted of proton exchange membrane, catalyst layers, micro porous layers and gas diffusion layers (GDL).

The bipolar plates distribute the reactant gas, expel the product water, collect current and provide the mechanical support of MEA, thereby playing a critical role in a PEMFC stack. An appropriate flow field is necessary for bipolar plates to implement the above functions effectively. The widely used

conventional flow fields in commercial bipolar plates, e.g., parallel, serpentine and interdigitated flow fields, have some kind of rib-channel structures [4]. Such configuration has limited capability to increase the power density of PEMFC, since it is apt to cause non-uniform gas and liquid water distributions in the electrodes and intricate to fabricate [5]. In order to further improve the performance of PEMFC, it is compulsory to design novel flow field configurations that can avoid the defects of the rib-channel structures.

Porous flow fields especially porous metal materials have been recognized as a promising substitute for the conventional flow field and have attracted increasing attention recently [6]. A variety of metal foams made of nickel [7-14], copper [15, 16], aluminum [17, 18], stainless steel [19] and nickelchromium [19, 20] as well as several metal sinters [21-25] have been explored experimentally to be used as flow fields of PEMFC. Besides, a volume of computational work [25-32] also exhibited that porous flow fields tended to achieve more uniform gas, temperature and current density distributions than conventional rib-channel flow fields. In the meantime, they could enhance the heat and water managements, thereby improving the performance of PEMFC. Obviously, the majority of the previous research focused on metal foam, while another porous metal material, i.e., metal fiber felt (MFF) received only scant attention. MFFs are made of micron order metal fibers which are non-woven, laminated and sintered at high temperatures. They play an important role in the filtration industry. Similar to metal foams, they have many favorable properties such as unique 3D porous structure, high electrical and thermal conductivity, and good manufacturability if used as flow fields of PEMFC, nevertheless few studies have been reported on such application. Gamburzev et al. [21] demonstrated that stainless steel fiber felt flow field achieved lower performance than traditional parallel flow fields, which largely resulted from the oxide film on the surface of stainless steel fiber felt. Tang et al. [24] concluded that the performance of the fuel cell with the porous copper fiber felt flow field was comparable with that of the serpentine flow field fuel cell, and it could get further improved if the copper fiber felt was optimized and the corrosion problem was successfully resolved. Li et al. [25] reported that when a copper fiber felt with the porosity of 70% was used as the flow field, the performance of the PEMFC was similar to that with serpentine flow field.

According to the research mentioned above, the MFFs seem to be a passable flow field if not worse compared with traditional rib-channel structure. However, it should be noted that all the MFFs in these research were used without being deposited any corrosion-resistant coating. The oxidation film on the surface of metal fibers might have adverse impact on the performance of PEMFC, covering up the fact that the porous structure of MFF flow fields could have performed better. Therefore, the MFFs need to be further examined to verify whether they are viable alternatives to conventional rib-channel flow field. In this work, the most common and the lowest cost MFF, i.e., commercial stainless steel fiber felt (CSSFF) was investigated. Five types of CSSFFs with various pore sizes and porosities were used as flow fields of PEMFC and compared with conventional serpentine flow field. The emphasis of this work was to investigate the structure feasibility of CSSFF as flow field and explore the effect of the CSSFF structures on the performance of PEMFC. Therefore, all CSSFFs were plated with gold to enhance their corrosion resistance and electrical conductivity, eliminating the adverse impact of badly conductive passive film on their surfaces.

2. EXPERIMENTAL

2.1. Physical characterization of the CSSFF

The CSSFF is produced by uniformly mixing and spreading stainless steel 316L fibers with certain distribution of length and diameter. This felt is then sintered in a reductive gas to obtain the porous metal fiber material. In the present study, five types of CSSFFs (Xi'an Filter Metal Materials Co., Ltd., China) were adopted. They are BZ10D, BZ20D, BZ40D, BZ60D and BZ100D, which are named by the manufacturer according to their average filtration rating. All the CSSFFs were plated with gold to eliminate the effect of passive film. The morphological features of the CSSFFs were inspected by a field emission scanning electron microscope (JSM-6700F, JEOF, Japan) to characterize the detailed microstructures which have a close relationship with the physical characteristics of the CSSFFs.

The porosities and pore sizes of the CSSFFs were measured by Archimedes principle-gas expansion replacement method (BSD-TD, BSD Instrument, China) and bubble point method (BSD-PB, BSD Instrument, China), respectively. In-plane conductivity was measured by four-point probe technique with the probe diameter of 1.0 mm. The interfacial contact resistance (ICR) between the CSSFFs and carbon paper was measured by methods well described in the literature [33].

2.2. Preparation of single PEMFC

Single PEMFC were utilized for the experiments in this study. Fig. 1 shows the close-up view and the schematic diagram of single PEMFC with CSSFFs as the flow fields. The single PEMFC included membrane electrode assembly (MEA), graphite separators, CSSFF flow fields, collector plates, insulating plates and end plates. The MEA employed in this study were made of seven layers including the anode gas diffusion layer (GDL), the anode micro porous layer (MPL), the anode catalyst layer (CL), the proton exchange membrane (PEM), the cathode CL, the cathode MPL and the cathode GDL. GORESELECT polymer membrane (W. L. Gore & Associates, Inc., the USA) was used as the electrolyte membrane for all MEAs. Catalyst layers (Johnson Matthey, UK) were coated on both sides of the membrane with the reaction area of 25 cm^2 (50 mm × 50 mm). The catalyst loading was 0.24 $mg \cdot cm^{-2}$ and 0.48 $mg \cdot cm^{-2}$ on the anode side and cathode side, respectively. Carbon paper of TGP-H060 (Toray Industries, Inc., Japan) with thickness of 0.19 mm was used as GDL on both sides of MEA. Gaskets were placed around the GDLs to prevent gas leakage. Grooves with a depth of 0.5 mm and an area of 25 cm^2 were formed in the graphite separator. The CSSFFs were cut to 50 mm × 50 mm size of square shape and inserted into the grooves.

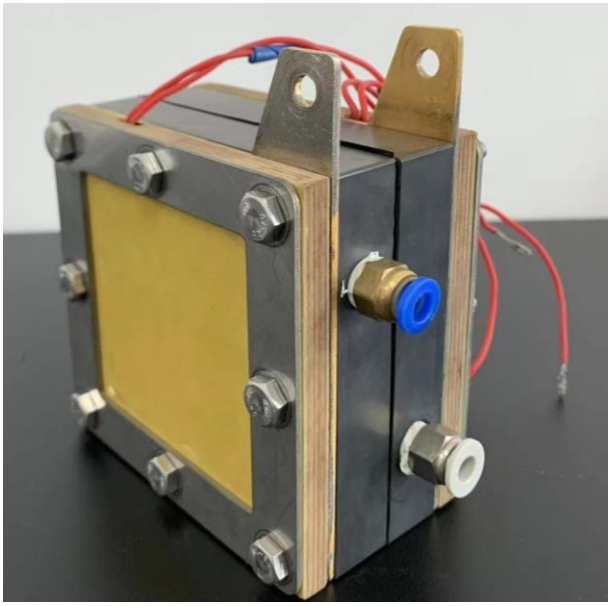

(a)

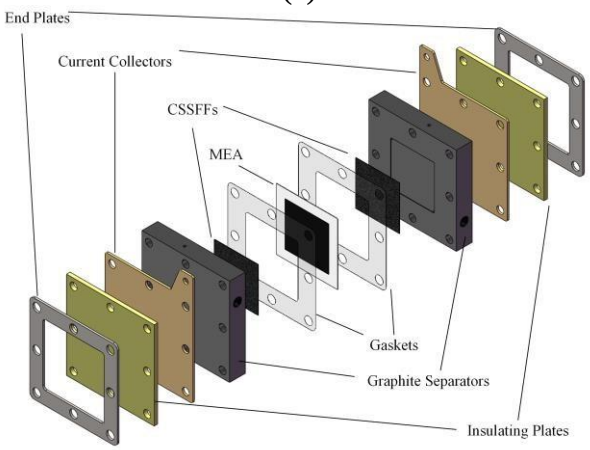

(b)

Figure 1. (a) Close-up view of the assembled single PEMFC, (b) Schematic of the configuration of single PEMFC with CSSFF flow fields.

Fig. 2 presents the photographs of the graphite separators with different flow fields. Fig. 2(a) shows a conventional serpentine flow field with a channel width of 1 mm and a channel depth of 1 mm. Fig. 2(b) shows the gold-plated CSSFF flow field. The inlet and outlet of the gas flow are located at diagonal corners. The thickness of the CSSFF was compressed to 0.5 mm when assembling the PEMFC, which is equal to the depth of the groove.

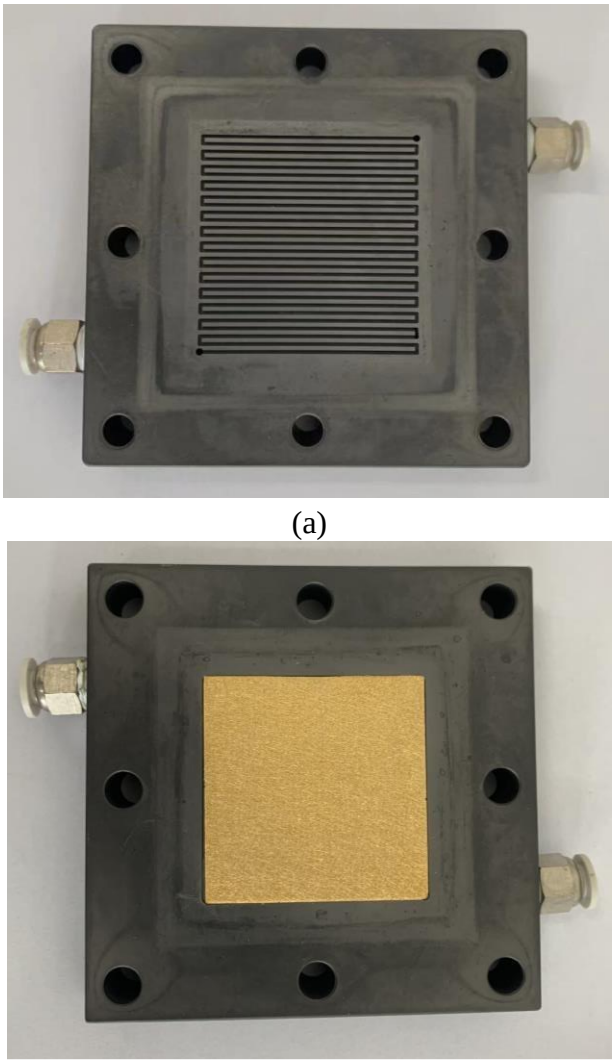

(a)

(b)

Figure 2. Photographs of (a) conventional serpentine flow field with a channel width of 1 mm and a channel depth of 1 mm, (b) gold-plated CSSFF flow field with a thickness of 0.5 mm.

2.3. Electrochemical characterization of PEMFC

The cyclic voltammetry (CV) measurement was performed to characterize the effective electrochemical surface area (ECSA) of the PEMFC with different flow fields, ensuring the consistency of MEAs among all the experiments. Prior to CV measurement, purging was carried out with N_2 for 20 minutes to remove air from the fuel cell. After purging, the PEMFC operated with 0.5 standard liter per minute (SLPM) fully-humidified hydrogen and 1.0 SLPM fully-humidified nitrogen supplied to the anode and cathode, respectively, for 20 minutes. Then CV was performed within a voltage range of 0.01-1.2 V and at a scan rate of 10 mV s^{-1}.

The performance of the single PEMFC with different flow fields was evaluated by measuring polarization curves using a fuel cell test system (FC-100W, Ningbo BaTe Technology Co., Ltd., China) under the operating conditions listed in Table 1. In this paper, stoichiometric ratio means the ratio between the actual flow rate of a reactant at the fuel cell inlet and the consumption rate of that reactant.

It should be pointed out that before conducting a fuel cell test, the MEA was hydrated to be activated and guarantee a steady performance. In addition, all values in this study were recorded when they were in a steady state.

Table 1. Operating conditions used in the experiments

Parameters	Values
Operating temperature	343.15 K
Relative humidity of inlet air	100%
Relative humidity of inlet hydrogen	100%
Air pressure	100 kPa, 140 kPa
Hydrogen pressure	100 kPa, 140 kPa
Stoichiometric ratio of air [a]	2
Stoichiometric ratio of hydrogen [b]	2

[a] the ratio between the actual flow rate and the consumption rate of air.

[b] the ratio between the actual flow rate and the consumption rate of hydrogen.

As the fuel cell runs, more and more liquid water will accumulate in the porous flow fields if it cannot be expelled promptly. The water will clog the pores of the CSSFFs, resulting in performance degradation of PEMFC. Therefore, the stability of fuel cells with CSSFF flow fields needs to be tested. In this work, the stability testing was carried out by measuring the voltage of the fuel cell at a constant high current density for an hour.

Electrochemical impedance spectroscopy (EIS) was conducted by an electrochemical workstation (PGSTAT302N, Metrohm Autolab, Switzerland) to measure the resistances of the single PEMFC. The impedance spectra were recorded as frequency swept from 10 kHz to 0.1 Hz. The applied AC current amplitude was fixed as 10% of the DC current produced by the fuel cell. The EIS measurements were performed at the current densities of 0.3 $A \cdot cm^{-2}$, 0.7 $A \cdot cm^{-2}$ and 1.3 $A \cdot cm^{-2}$ for the single cells with different flow fields to compare the losses of fuel cells operating at low, medium, and high current densities, respectively. Apart from that, the EIS measurements were also carried out at different current densities for the fuel cell with BZ100D flow field to show how the resistances of PEMFC changed with current density.

3. RESULTS AND DISCUSSION

3.1. Physical properties of the CSSFFs

Fig. 3 shows morphological features of the five CSSFF samples. Fig. 3(a) - 3(e) presents the top views of BZ10D, BZ20D, BZ40D, BZ60D, and BZ100D, respectively. As a representative, Fig. 3(f) shows the cross-section of BZ100D. As can be seen from Fig. 3, the CSSFF has a layered structure in which stainless steel fibers with diameters of 12 μm and/or 22 μm are intricately entangled and overlapped. It is apparent that all the pores inside are connected, which is beneficial to transport the reactant gas and liquid water. Since the stainless steel fibers are randomly distributed in orientation during the sintering process, the irregular pores formed by them are not arranged evenly.

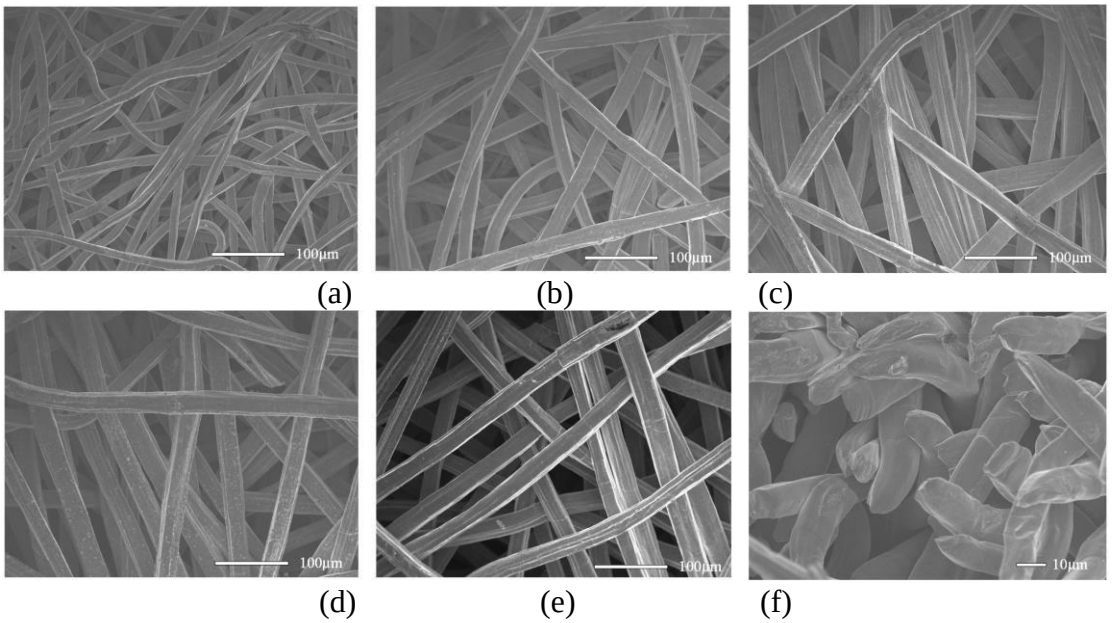

Figure 3. SEM images of CSSFFs, (a) BZ10D with 76.2% porosity, (b) BZ20D with 77.4% porosity, (c) BZ40D with 80.1% porosity, (d) BZ60D with 81.6% porosity, (e) BZ100D with 85.7% porosity, (f) cross-section of BZ100D with 85.7% porosity.

Table 2 displays the physical properties of the CSSFFs measured in this work, including thickness, average pore diameter, porosity and in-plane electrical resistivity. The thickness of these CSSFFs ranges from 0.52 mm to 0.67 mm, which will result in different levels of compression when they are inserted into the 0.5-millimeter-depth groove of the graphite separator. BZ100D has the largest pore size and porosity among all the CSSFFs. Specifically, the average pore diameter of BZ100D is six times larger than that of BZ10D. The in-plane electrical resistivity increases with the porosity and average pore diameter of the CSSFFs.

Table 2. Physical properties of the CSSFFs

Type	Thickness/mm	Average pore diameter/μm	Porosity	In-plane electrical resistivity/mΩ·cm
BZ10D	0.62	12.3	76.2%	0.70
BZ20D	0.55	24.7	77.4%	0.72
BZ40D	0.65	51.6	80.1%	0.90
BZ60D	0.52	71.7	81.6%	0.98
BZ100D	0.67	86.4	85.7%	1.14

Compared with in-plane resistivity, contact resistance has a much greater effect on cell performance.

Fig 4 shows the measured contact resistance at various compaction pressures between the original CSSFFs and carbon paper. The original BZ100D presents the smallest contact resistance all the time among these CSSFFs. Its contact resistance is approximately 200 mΩ·cm^2 at 1.5 MPa. While the contact resistance between the copper fiber felt and the carbon paper is about 3.0 mΩ·cm^2 [24], which is much smaller than that of the original BZ100D. Gold plating can dramatically reduce the contact resistance. As shown in Fig. 4, the contact resistances between the gold-plated CSSFFs and carbon paper decrease to values smaller than 0.025 mΩ·cm^2 even at compaction pressures as low as 0.6 MPa, which is beyond the measuring range of the instrument.

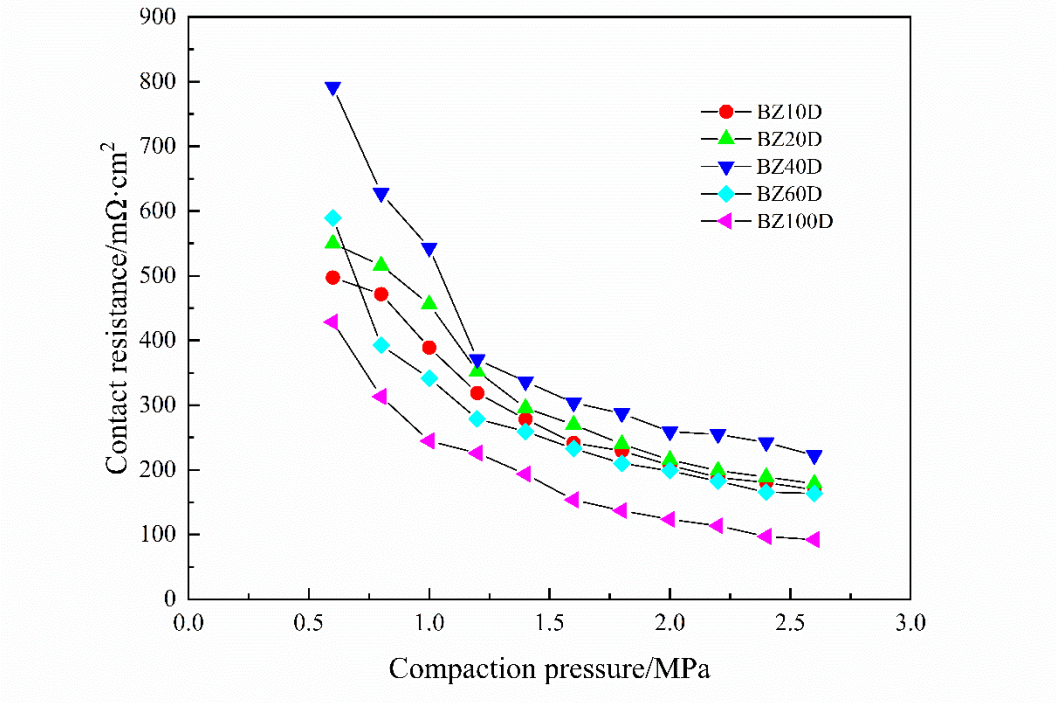

Figure 4. Contact resistance between the original CSSFFs and carbon paper at various compaction pressures.

3.2. PEMFC performance

The measured CV curves of PEMFC with different flow fields are shown in Fig. 5. The ECSA of the MEA is basically the same. Hence, the difference of cell performance is mainly attributed to the use of the CSSFFs as the flow fields.

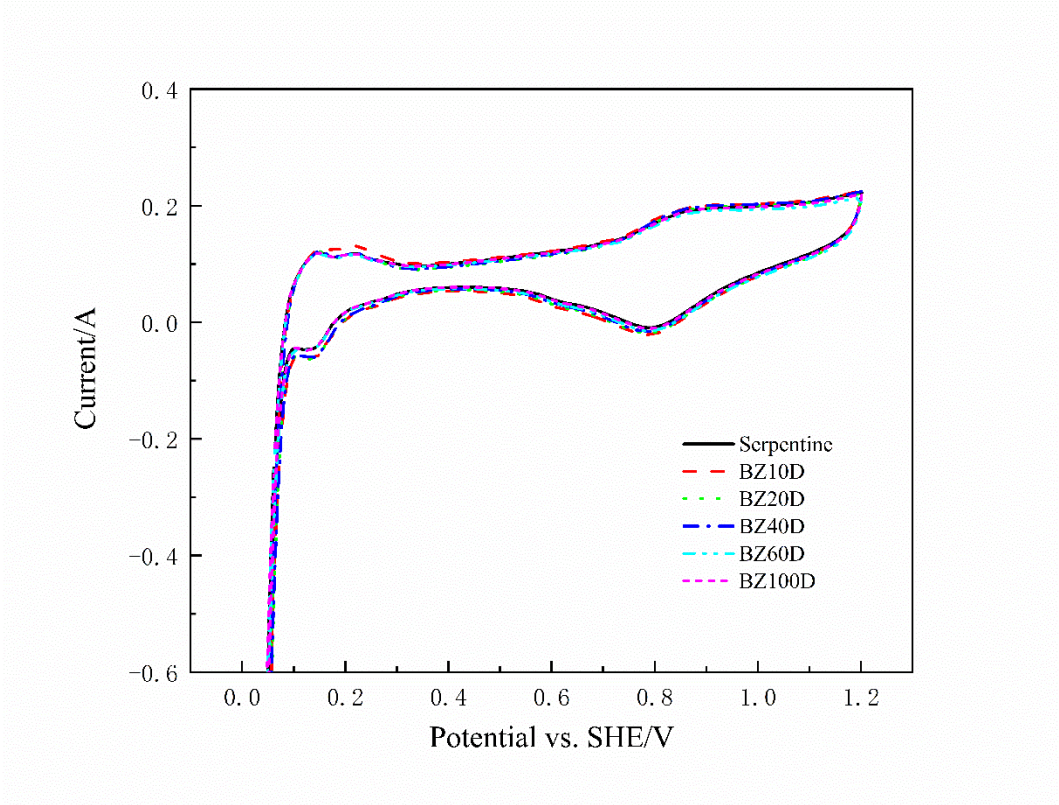

Figure 5. Comparison of cyclic voltammograms of fuel cells with conventional serpentine and CSSFF flow fields at hydrogen feeding rate of 0.5 SLPM and nitrogen feeding rate of 1.0 SLPM.

Fig. 6 shows polarization curves of fuel cells with serpentine and CSSFF flow fields at the operating pressures of 100 kPa and 140 kPa. The first thing to state is that when BZ10D and BZ40D are utilized, the stoichiometry ratio of air has to be larger than 4 to keep the fuel cell running normally. The possible reason is that BZ10D and BZ40D are compressed seriously during the assembling of the fuel cells, therefore, more air is needed to expel the liquid water. As can be seen from Fig. 6, the voltages of fuel cells with CSSFF flow fields are always higher than that of serpentine flow field. As expected, the performances of fuel cells are improved when the operating pressure increases, as shown in Fig. 6(b). Every fuel cell using CSSFF as a flow field shows higher current density than 1.6 $A \cdot cm^{-2}$ when it operates at a constant voltage of 0.6 V. Especially, the fuel cell with BZ100D flow field exhibits the best performance, generating approximately 2.0 $A \cdot cm^{-2}$ at 0.6 V, while the current density of serpentine flow field fuel cell is merely 0.8 $A \cdot cm^{-2}$. Therefore, fuel cells with CSSFF flow fields generate much more current than conventional rib-channel flow field fuel cell.

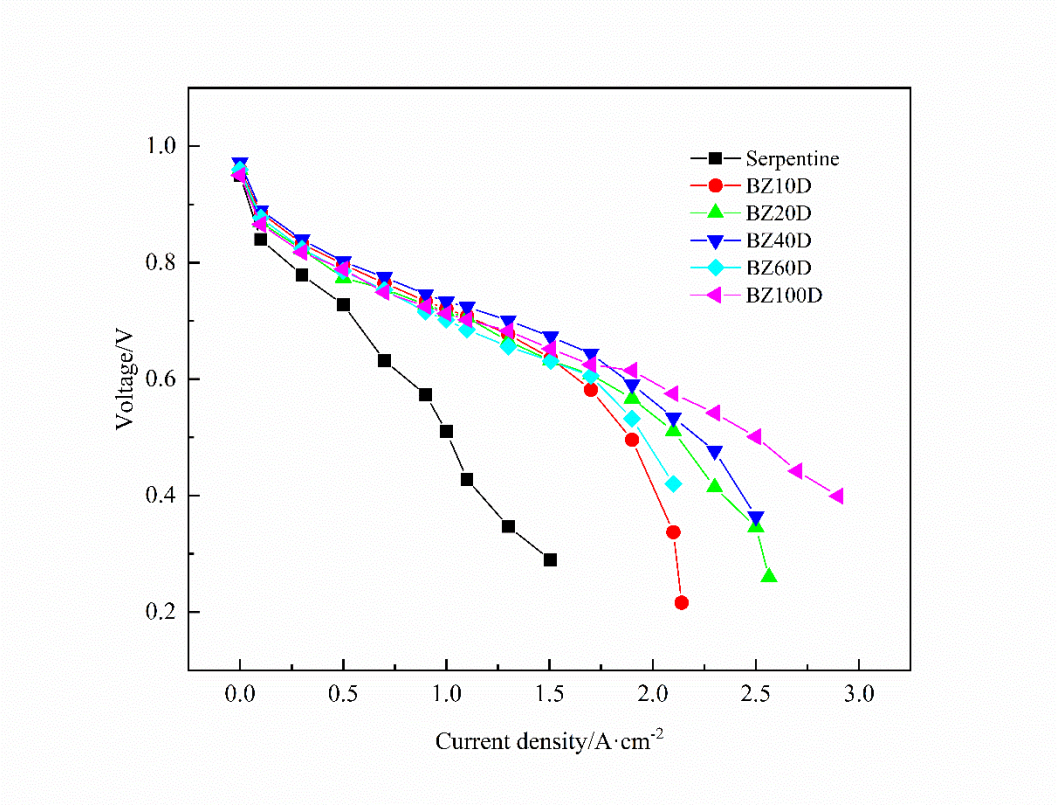

（a）

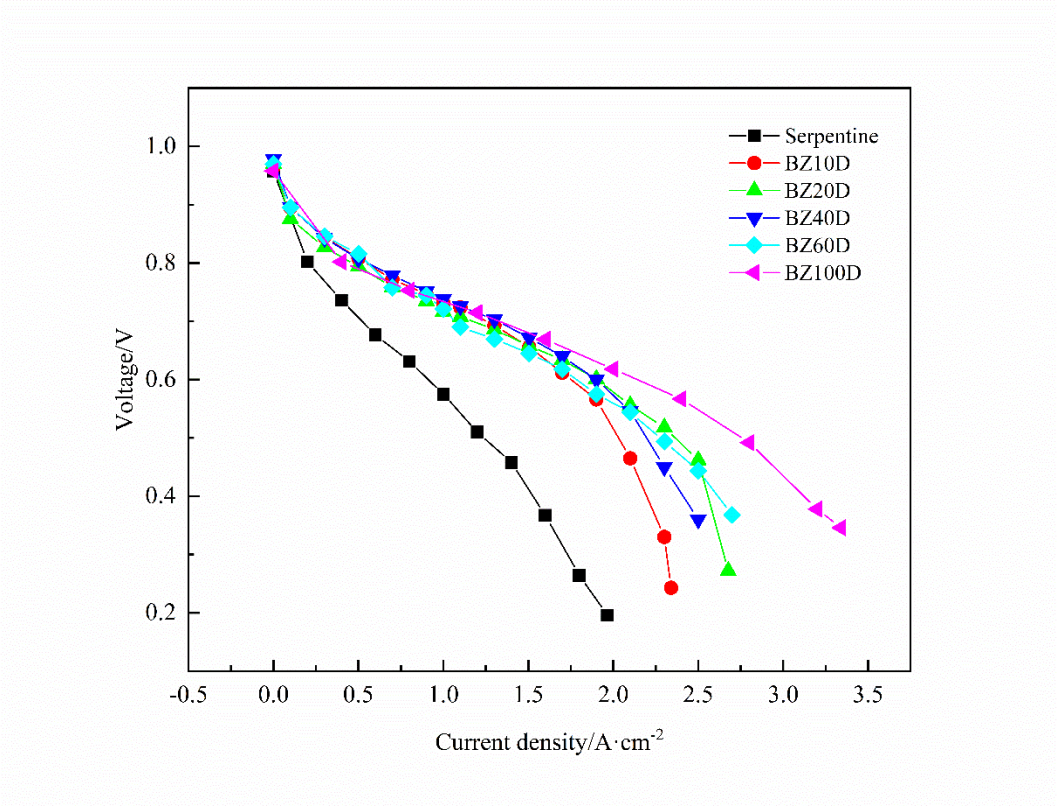

(b)

Figure 6. Polarization curves of PEMFC with conventional serpentine and CSSFF flow fields at 100% relative humidity, 343.15 K operating temperature and the operating pressures of (a) 100 kPa, (b) 140 kPa.

The performances of various CSSFFs are very close when the current density is lower than 1.0 A·cm^{-2}, while the differences become obvious at high current density. It should be noted that larger pore size doesn't necessarily mean better performance. For example, fuel cell with BZ20D flow field generates higher current density than that with BZ60D flow field.

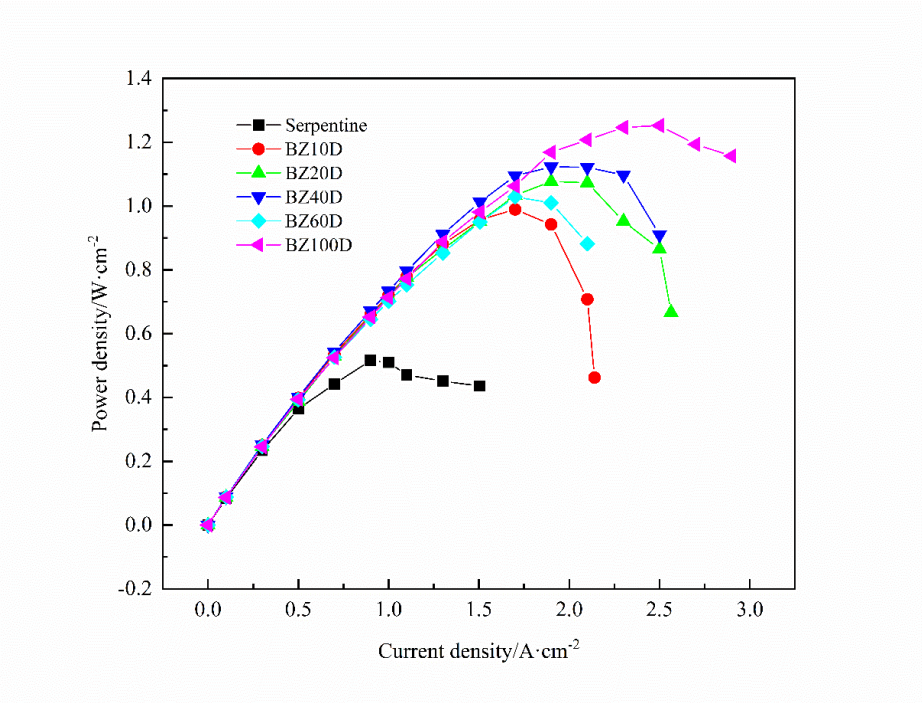

(a)

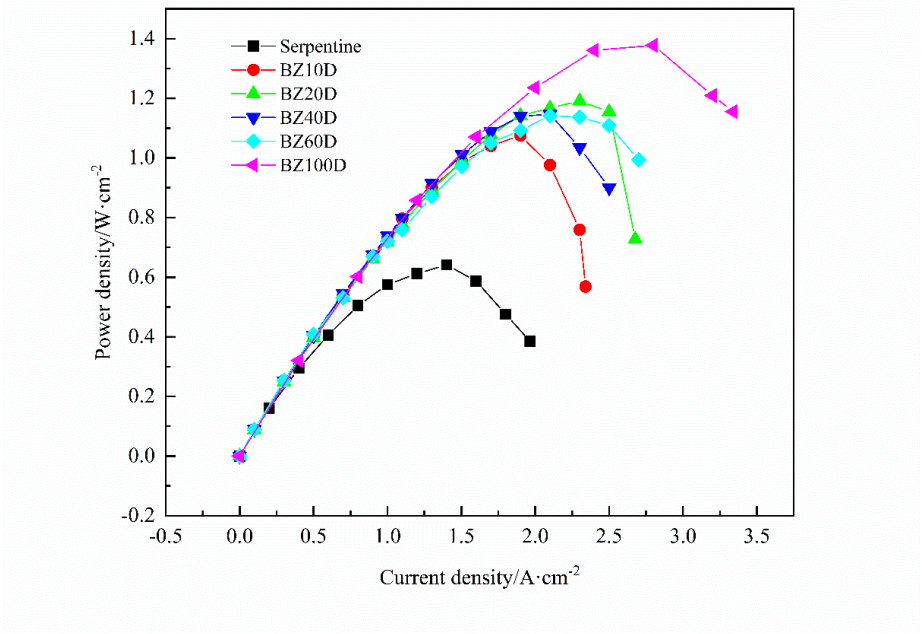

(b)

Figure 7. Power density curves of PEMFC with conventional serpentine and CSSFF flow fields at 100% relative humidity, 343.15 K operating temperature and the operating pressures of (a) 100 kPa, (b) 140 kPa.

Fig. 7 shows the power density curves of PEMFC with serpentine and CSSFF flow fields at the operating pressures of 100 kPa and 140 kPa. Fuel cells with CSSFF flow fields produce much more power than that with conventional serpentine channel. To be specific, when it comes to maximum power density at the operating pressure of 100 kPa, fuel cell with BZ100D flow field generates about 1.25 $W \cdot cm^{-2}$ at 2.5 $A \cdot cm^{-2}$ while conventional serpentine channel produces merely 0.52 $W \cdot cm^{-2}$ at 0.9 $A \cdot cm^{-2}$. Therefore, the results indicate that the performance of fuel cell can be improved significantly by using CSSFFs as flow fields. This is consistent with the conclusion made by Tsai et al. [8], Liu et al. [13] and Park et al. [15], and their results illustrate that the performance of porous metal flow field is much higher than that of the conventional rib-channel flow field.

Previous research [21, 24, 25] suggests that PEMFC with MFF flow field performs no better than conventional rib-channel flow field. However, the experimental results in this work indicate that CSSFF flow field can improve the performance of PEMFC significantly. It needs to be emphasized that these work is not contradictory. In this study, the CSSFFs are plated with gold, which can reduce the contact resistance between the flow field and GDL dramatically as well as improve the corrosion resistance of stainless steel effectively. Nevertheless, the copper and stainless steel fiber felts without any surface treatment are utilized in previous work [21, 24, 25]. In the acid environment of PEMFC, the badlyconductive oxidation film will form on the surface of the untreated MFF, thus reducing the performance of the fuel cell.

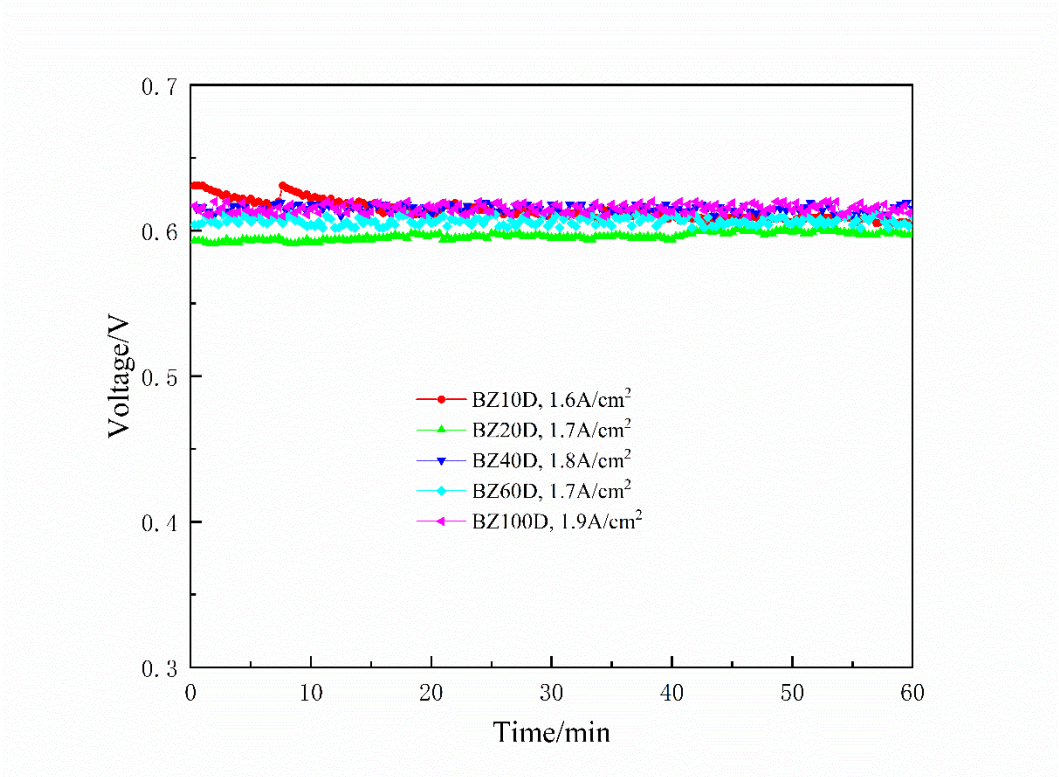

Figure 8. Voltage measurement for one hour period for PEMFC with different CSSFF flow fields at 100% relative humidity, 343.15 K operating temperature and 100 kPa operating pressure.

As already mentioned above, the stability testing of fuel cells with different CSSFF flow fields was conducted at certain current densities for an hour and fluctuations of voltages were recorded to

verify their stability. The current densities were determined to keep the voltages of the fuel cells at around 0.6 V. They were 1.6 A·cm^{-2}, 1.7 A·cm^{-2}, 1.8 A·cm^{-2}, 1.7 A·cm^{-2} and 1.9 A·cm^{-2} for BZ10D, BZ20D, BZ40D,

BZ60D and BZ100D, respectively. As presented in Fig. 8, the voltages of all fuel cells don't change much during one hour period, indicating that the liquid water produced in the electrodes can be expelled in time and the fuel cells can operate stably.

3.3. Electrochemical Impedance Spectroscopy

As shown in Fig. 6 and Fig. 7, CSSFFs generally exhibit higher levels of performance than serpentine flow field and BZ100D performs the best, especially in the high current density region where mass transfer resistance dominates. To better elucidate the results, EIS measurement was conducted. Fig. 9 shows Nyquist plots for each fuel cell at current densities of 0.3 A·cm^{-2}, 0.7 A·cm^{-2}, and 1.3 A·cm^{-2}, respectively. The intersection of the real axis at high frequency implies the total internal ohmic resistance of the fuel cell including the contact resistance and ohmic resistance of cell components such as the graphite separators, CSSFFs and MEA. Fig. 9(a) is the Nyquist plot measured at the current density of 0.3 A·cm^{-2}, at which point contributions of mass transfer resistance are limited. It is important to note that serpentine flow field possesses the highest ohmic resistance (4 mΩ - 5 mΩ) at high frequencies while the CSSFFs present relatively low levels of ohmic resistance (2 mΩ - 3 mΩ). As fuel cell performance was measured under the same conditions, different ohmic resistances observed are considered to originate from the difference in flow fields. CSSFFs form a porous structure by overlapping stainless steel fibers, resulting in larger contact area than serpentine flow field, thereby lowering their ohmic resistances.

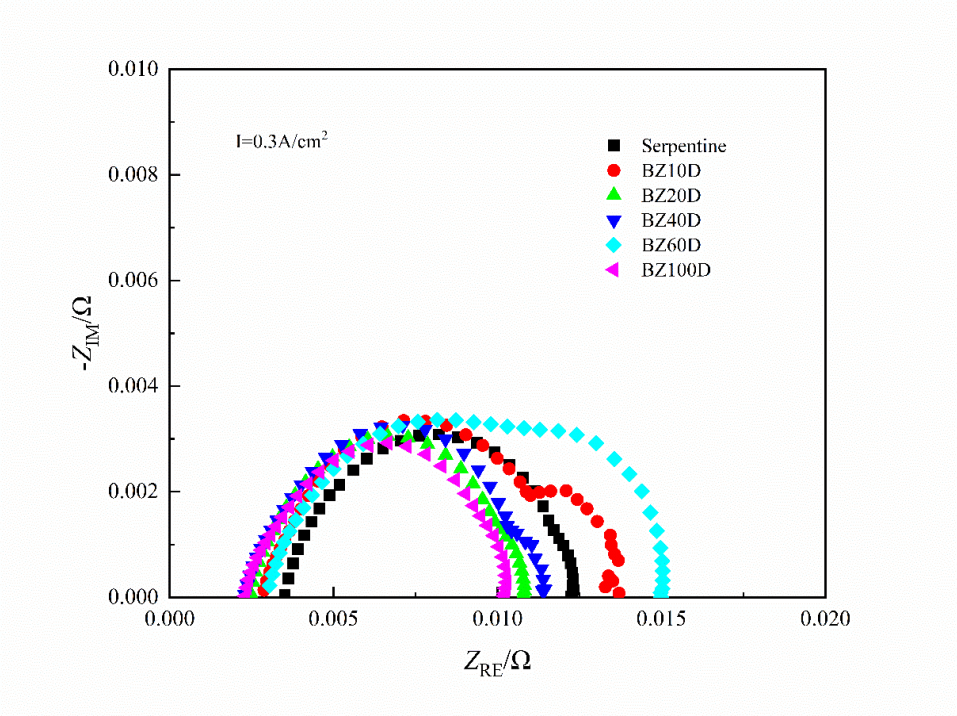

(a)

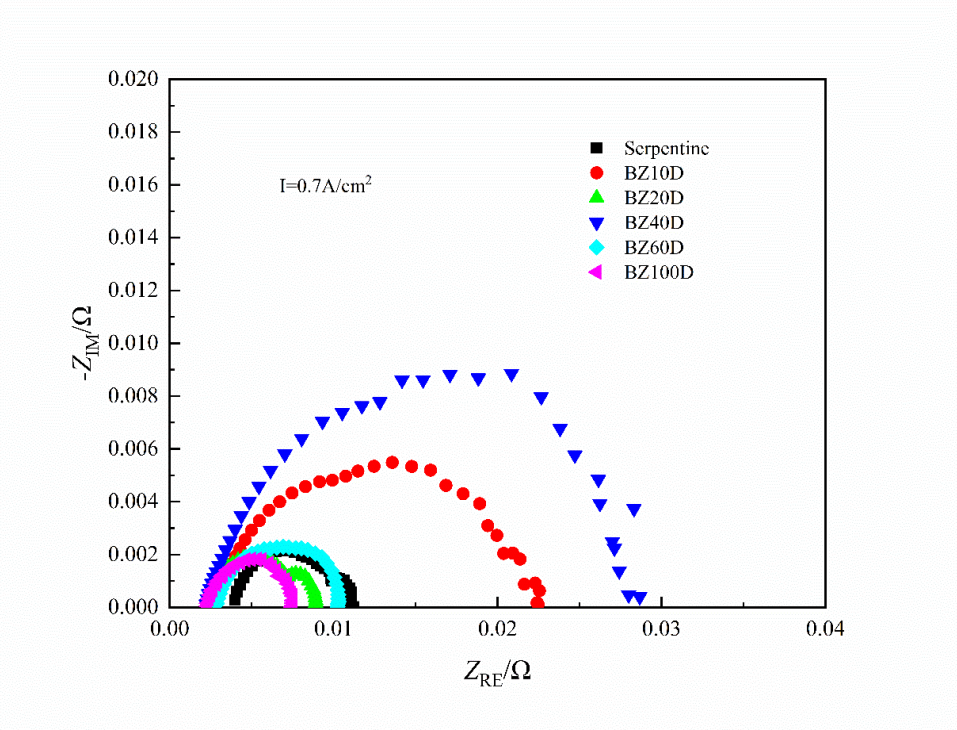

(b)

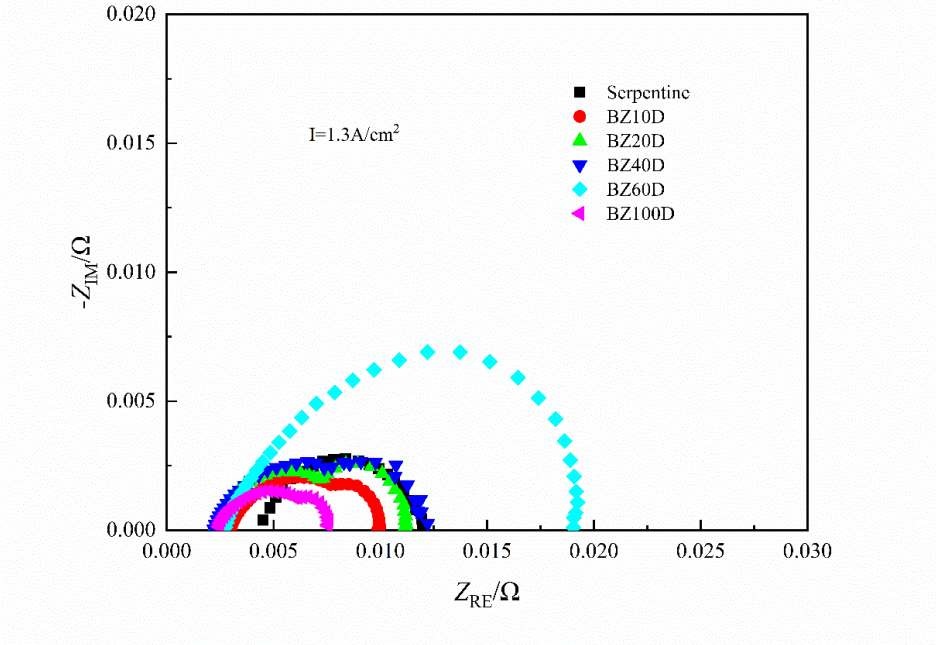

(c)

Figure 9. Nyquist plots for the fuel cells with different flow fields under various current densities, (a) 0.3 A·cm^{-2}, (b) 0.7 A·cm^{-2}, (c) 1.3 A·cm^{-2}.

Fig. 9(c) is the Nyquist plot measured at the current density of 1.3 A·cm^{-2}, at which the level of mass transfer resistance is critical. When the mass transfer is dominant, the size of the semicircle

measured at low frequency is dependent on the mass transfer resistance. Apparently, BZ100D flow field improves the rate of mass transfer significantly in PEMFC, which contributes to achieving the most excellent performance in high current density regions.

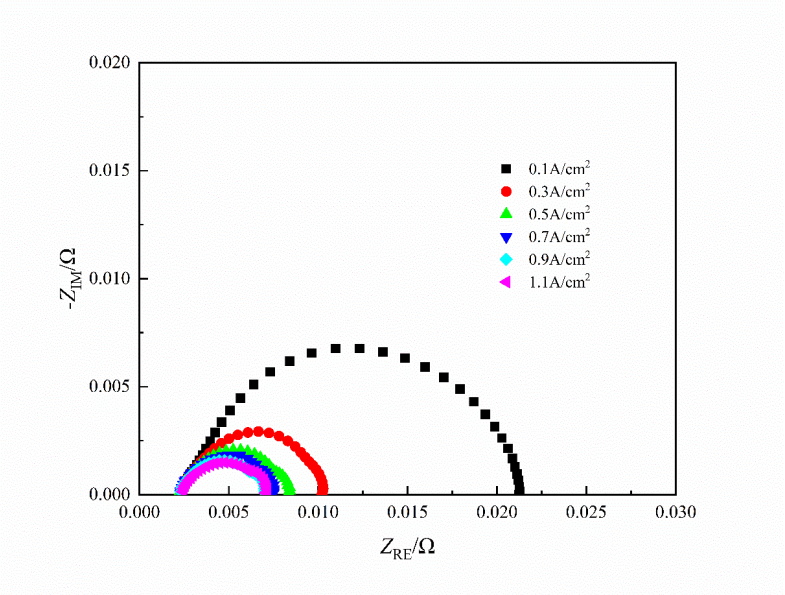

(a)

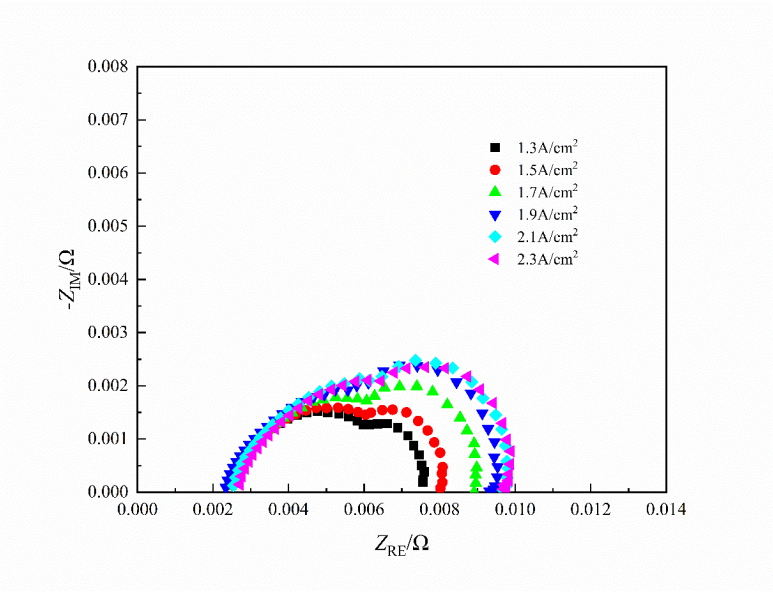

(b)

Figure 10. Nyquist plots for the fuel cell with BZ100D flow field under various current densities, (a) 0.1 A·cm^{-2}-1.1 A·cm^{-2}, (b) 1.3 A·cm^{-2}-2.3 A·cm^{-2}

Fig. 10 shows the Nyquist plots of the BZ100D flow field fuel cell at different current densities. From Fig. 10(a), it can be seen that at low and medium current densities, the intersection point of the low frequency part with the real axis, i.e., the total cell resistance, decreases with increasing current density. Compared to the high and low frequency arcs, the medium frequency arc, i.e., the cathode activation loss, is larger and dominated, and it decreases with increasing current density. As shown in Fig. 10(b), as the current density increases from 1.3 A·cm^{-2} to 2.3 A·cm^{-2}, the diameters of the medium and low frequency arcs continue to increase. And the size of low frequency arc gradually exceeds that

of the medium frequency arc, which means the mass transfer loss gradually dominates. These results are quite similar to those presented by Park et al. [15].

4. CONCLUSION

In this work, the structure feasibility of MFFs as flow fields for PEMFC was explored experimentally. Five types of gold-plated CSSFFs with different pore sizes and porosities, i.e., BZ10D, BZ20D, BZ40D, BZ60D and BZ100D were investigated. Based on the measured polarization curves, power density curves and electrochemical impedance results, the main conclusions of this study can be summarized as follows:

(1) CSSFFs with conductive and corrosion resistant coatings could be viable alternatives to conventional rib-channel flow field.

(2) Compared with conventional serpentine flow field, the performances of PEMFC with CSSFF flow fields are improved significantly. In particular, fuel cell with BZ100D flow field which has the largest pore size and the highest porosity performs the best among all CSSFFs, generating about 2.0 $A \cdot cm^{-2}$ at 0.6 V, and the maximum power density is approximately 1.25 $W \cdot cm^{-2}$ at 2.5 $A \cdot cm^{-2}$.

(3) Fuel cells with CSSFF flow fields can operate stably and they generally exhibit lower ohmic resistance than that with serpentine flow field. BZ100D flow field can improve the rate of mass transfer dramatically in PEMFC, which contributes to achieving the most excellent performance in high current density regions.

ACKNOWLEDGEMENTS
This work was supported by Enterprise Top Innovative Young Talents Support Plan and Xi'an Postdoctoral Innovation Base.

References

1. A. Gong and D. Verstraete, *Int. J. Hydrogen Energy*, 42 (2017) 21311.
2. M. Kandidayeni, J.P. Trovão, M. Soleymani and L. Boulon, *Int. J. Hydrogen Energy*, 47 (2022) 10021.
3. M. Li, Y. Bai, C. Zhang, Y. Song, S. Jiang, D. Grouset and M. Zhang, *Int. J. Hydrogen Energy*, 44 (2019) 10677.
4. A.P. Manso, F.F. Marzo, J. Barranco, X. Garikano and M.G. Mujika, *Int. J. Hydrogen Energy*, 37 (2012) 15256.
5. K. Jiao and X. Li, *Prog. Energy Combust. Sci.*, 37 (2011) 221.
6. Y. Zhang, Y. Tao and J. Shao, *J. Power Sources*, 492 (2021) 229664.
7. F.P. Ting, C.W. Hsieh, W.H. Weng and J.C. Lin, *Int. J. Hydrogen Energy*, 37 (2012) 13696.
8. B.T. Tsai, C.J. Tseng, Z.S. Liu, C.H. Wang, C.I. Lee, C.C. Yang and S.K. Lo, *Int. J. Hydrogen Energy*, 37 (2012) 13060.
9. Y. Tabe, T. Nasu, S. Morioka and T. Chikahisa, *J. Power Sources*, 238 (2013) 21.
10. S. Huo, N.J. Cooper, T.L. Smith, J.W. Park and K. Jiao, *Appl. Energy*, 203 (2017) 101.
11. M. Kim, C. Kim and Y. Sohn, *Fuel Cells*, 18 (2018) 123.
12. D.K. Shin, J.H. Yoo, D.G. Kang and M.S. Kim, *Renewable Energy*, 115 (2018) 663.

13. R. Liu, W. Zhou, S. Li, F. Li and W. Ling, *Int. J. Hydrogen Energy*, 45 (2020) 17833.
14. Y. Wu, J.I.S. Cho, M. Whiteley, L. Rasha, T.P. Neville, R. Ziesche, R. Xu, R. Owen, N. Kulkarni, J. Hack, M. Maier, N. Kardjilov, H. Markötter, I. Manke, F.R. Wang, P.R. Shearing and D.J.L. Brett, *Int. J. Hydrogen Energy*, 45 (2020) 2195.
15. J.E. Park, W. Hwang, M.S. Lim, S. Kim, C.Y. Ahn, O.H. Kim, J.G. Shim, D.W. Lee, J.H. Lee, Y.H. Cho and Y.E. Sung, *Int. J. Hydrogen Energy*, 44 (2019) 22074.
16. C.Y. Ahn, M.S. Lim, W. Hwang, S. Kim, J.E. Park, J. Lim, I. Choi, Y.H. Cho and Y.E. Sung, *Fuel Cells*, 17 (2017) 652.
17. Y. Awin and N. Dukhan, *Appl. Energy*, 252 (2019) 113458.
18. M.S. Hossain and B. Shabani, *Int. J. Hydrogen Energy*, 44 (2019) 25905.
19. A. Kumar and R.G. Reddy, *J. Power Sources*, 129 (2004) 62.
20. G.W. Lee, G.H. Shim, J.M. Kim, C. Seol, J.H. Kim, S.M. Kim and H.S. Ahn, *Int. J. Hydrogen Energy*, 45 (2020) 12972.
21. S. Gamburzev and A.J. Appleby, *J. Power Sources*, 107 (2002) 5.
22. M. Kozakai, K. Date, Y. Tabe and T. Chikahisa, *Int. J. Hydrogen Energy*, 41 (2016) 13180.
23. T. Kariya, T. Hirono, H. Funakubo and T. Shudo, *Int. J. Hydrogen Energy*, 39 (2014) 15072.
24. Y. Tang, W. Yuan, M. Pan and Z. Wan, *Int. J. Hydrogen Energy*, 35 (2010) 9661.
25. S. Li, W. Zhou, R. Liu, J. Huang and X. Chu, *Curr. Appl. Phys.*, 20 (2020) 686.
26. J.E. Park, J. Lim, S. Kim, I. Choi, C.Y. Ahn, W. Hwang, M.S. Lim, Y.H. Cho and Y.E. Sung, *Electrochim. Acta*, 265 (2018) 488.
27. E. Afshari, *J. Therm. Anal. Calorim.*, 139 (2020) 2423.
28. Z. Bao, Z. Niu and K. Jiao, *Int. J. Hydrogen Energy*, 44 (2019) 6229.
29. A. Jo and H. Ju, *Int. J. Hydrogen Energy*, 43 (2018) 14012.
30. Y. Zhang, J. Shao and Y. Tao, *Int. J. Energy Res.*, 46 (2022) 1894.
31. M. Suo, K. Sun, R. Chen, Z. Che, Z. Zeng, Q. Li, X. Tao and T. Wang, *J. Power Sources*, 521 (2022) 230937.
32. M.J. Kermani, M.M. Jahromi, M. Hasheminasab, L. Wei, J. Guo and F. Jiang, *Int. J. Hydrogen Energy*, 47 (2022) 4772.
33. V. Mishra, F. Yang and R. Pitchumani, *J. Fuel Cell Sci. Technol.*, 1 (2004) 2.